Nanoscale Advances

Accepted Manuscript

This article can be cited before page numbers have been issued, to do this please use: J. Riaz, S. Knani, A. Bibi and M. Arif, *Nanoscale Adv.*, 2026, DOI: 10.1039/D6NA00134C.

ROYAL SOCIETY OF CHEMISTRY

rsc.li/nanoscale-advances

View Article Online
DOI: 10.1039/D6NA00134C

Enhanced Electrochemical Performance of $W_{18}O_{49}$/TiN Binary Composite Electrodes for Asymmetric Supercapacitors

Junaid Riaz [1], Muhammad Arif [1*], Salah Knani [2], Amina Bibi [3*]

Authorship: Junaid Riaz

Co-Authorship: Salah Knani

Corresponding Authorship: Muhammad Arif, Amina Bibi

[1] *Yunnan Key Laboratory of Optoelectronic Information Technology, School of Physics and Electronic Information, Yunnan Normal University, Kunming 650500, China.*

[2] *Center for Scientific Research and Entrepreneurship, Northern Border University, Arar 73213, Saudi Arabia..*

[3] *Department of Physics, Hazara University, Mansehra 21300, Pakistan.*

Email: junaidriaz1990@gmail.com, aminaamni11@gmail.com,

Abstract

To develop high-performance supercapacitors, this study produced and thoroughly characterized a TiN-$W_{18}O_{49}$ nanocomposite electrode. The successful production of the TiN-$W_{18}O_{49}$ nanocomposite, which combines the high electrical conductivity of TiN with the pseudocapacitive behavior of $W_{18}O_{49}$, was validated by structural and morphological investigations (XRD, SEM, BET, and EDX). The results of the electrochemical tests showed that the composite outperformed the parts used purely. Low solution resistance (Rs = 0.54 Ω) and a significantly reduced charge transfer resistance (Rct = 1.38 Ω) were observed by electrochemical impedance spectroscopy, suggesting effective electron transport and enhanced interfacial kinetics. Redox peaks were clearly visible in the potential window of 0.0-0.5 V at scan speeds of 50 $mV \cdot s^{-1}$ in cyclic voltammetry, and a high specific capacitance of 1482 $F \cdot g^{-1}$ at 1 $A \cdot g^{-1}$ was obtained in galvanostatic charge-discharge analysis. Asymmetric supercapacitor in the potential range of 1.3 V show 91.1 % of its initial capacitance retained after 10,000 cycles, the electrode demonstrated exceptional cycling stability. Furthermore, the TiN-$W_{18}O_{49}$//AC electrode achieved a maximum power density of 4564.9 $W \cdot kg^{-1}$ and an impressive energy density of 58.91 $Wh \cdot kg^{-1}$. Based on these findings, the TiN-$W_{18}O_{49}$ heterostructure is a potential electrode material for next-generation supercapacitors, due to the synergistic effect of the two materials.

View Article Online
DOI: 10.1039/D6NA00134C

Keywords: TiN-$W_{18}O_{49}$ nanocomposite, Asymmetric Supercapacitor, Energy Density, Power Density, Retentions

1. Introduction

Over the last few years, supercapacitors (SCs) have received an impressive attraction as effective energy storage systems that can produce high-power density, high-charge-discharge rates, and extended operating periods [1, 2]. They are very useful in the transition between traditional capacitors and batteries, so they are very applicable to portable electronics, electric vehicles, and renewable energy systems that utilize intermittent energy sources, including solar and wind energy. The inherent characteristics of electrode materials determine, to a large extent, the electrochemical performance of SCs because they determine their charge storage capacity, rate capability, and cycling durability [3, 4]. The transition metal oxides, including RuO_2, ZnO, Cu_2O, MnO_2, and Co_2O_3, are some of the other materials that have been examined with great enthusiasm due to their multiple oxidation states, extensive redox viability, and excellent pseudocapacitive properties [5-9].

Among metal oxides, tungsten oxide has attracted increasing attention as a pseudocapacitor electrode due to its high electronic conductivity, excellent structural stability, and ability to facilitate rapid ion insertion [10, 11]. In particular, monoclinic $W_{18}O_{49}$, which comprises tungsten in the W^{5+} oxidation state, has sufficient oxygen vacancies that reduce resistivity, increase ion transport, and enhance electrochemical activity, and thus is a promising electrode material in high-performance supercapacitors [10, 12]. WO_x deposited onto carbon cloth [13], and then electrophoretically coated with $Ti_3C_2T_x$ (WO_x@CC/$Ti_3C_2T_x$) delivered a capacitance of 164 F g^{-1} at 5 mA cm^{-2}. Patil et al. [14] reported a three-dimensional m-WO_3/$Ti_3C_2T_x$/hollow graphene foam electrode, which attained 573 F g^{-1} at 5 mV s^{-1}. $W_{18}O_{49}$ nanowire-rGO also possesses better capacitance, stability, and energy density in $AlCl_3$ electrolyte due to augmented ion diffusion and charge movement [15]. Moreover, the synthesis of Sn-doped $W_{18}O_{49}$ through a one-pot solvothermal method indicated that 3% Sn-$W_{18}O_{49}$ had a distinct 3D sea urchin-shaped structure with 546 F g^{-1} at 4 A g^{-1} and a retention of 86% after 6000 cycles [16]. An MXene/rGO/$W_{18}O_{49}$ film electrode (binder-free) had a 581.2 F g^{-1} at 1 A g^{-1} and an ASC energy density of 43.2 Wh kg^{-1} and a 87.1% retention after 10000 cycles [12]. On the same lines, FeS-$W_{18}O_{49}$ composite made by using a wet-chemical process provided a

View Article Online
DOI: 10.1039/D6NA00134C

discharge of 558 F g^{-1} at 1 A g^{-1} with 87.6 retention after 10000 cycles, which emphasizes the combined role of the conductivity of FeS and the redox capacity of $W_{18}O_{49}$ [17].

Based on the promising electrochemical characteristics of $W_{18}O_{49}$ -based composites, the addition of conductive transition metal nitrides like TiN can be further added to improve electrode performance. TiN has been recognized as very good in terms of electrical conductivity, chemical stability, and mechanical strength, which makes it easy to transport electrons and enhances the collection of the charges in composite electrodes [18-20]. Different TiN-composited materials have been demonstrated to show greater improvements in electrochemical performance because of the establishment of conductive networks and increased interfacial contact, like TiN/Ni [21], TiN/Vertical graphene [22], TiN/ZnS [23], TiN/MoS_2 [24], TiN/Fe_2O_3 [25], TiN/CuO [26], TiN/Al2O3 [27], and MnO_2/TiN [28]. TiN, when integrated with $W_{18}O_{49}$, can form a synergistic network that enhances the active surface area, exposes additional redox sites, and reduces internal resistance, thereby improving both capacitance and rate capability.

This work demonstrates that the TiN-$W_{18}O_{49}$ heterostructured nanocomposite effectively combines the high conductivity of TiN with the pseudocapacitive behavior of $W_{18}O_{49}$, resulting in outstanding electrochemical performance. The nanocomposite exhibits low solution resistance (R_s = 0.54 Ω) and reduced charge transfer resistance (R_{ct} = 1.38 Ω), facilitating efficient electron transport and enhanced interfacial kinetics. In the three-electrode system, it delivers a high specific capacitance of 1482 F·g^{-1} at 1 A·g^{-1} with clear redox peaks in the 0.0-0.5 V window. The TiN-$W_{18}O_{49}$//AC asymmetric supercapacitor maintains 91.1 % capacitance retention after 10,000 cycles, with a maximum energy density of 58.91 Wh·kg^{-1} and a power density of 4564.9 W·kg^{-1}. These results underscore the synergistic effect between TiN and $W_{18}O_{49}$, confirming the heterostructure as a promising electrode material for next-generation high-performance supercapacitors (for more details see table 8).

2. Materials and Synthesis

2.1 Materials

During the experimental procedure, we used the following chemicals: Titanium butoxide $Ti(C_4H_9O)_4$, Acetic acid (AcOH), Ammonia gas (NH_3), Tungsten hexachloride (WCl_6), Ethanol, polyvinylidene, n-methyl-2-pyrrolidone (NMP), Nickel foam, MnO_2 and carbon black (CB). These chemicals were purchased from Sinopharm chemical reagent Beijing Co.Ltd and were of analytical reagent grade; thus, they were used without further purification.

View Article Online
DOI: 10.1039/D6NA00134C

2.2 Synthesis and Preparation of $W_{18}O_{49}$, TiN, and TiN-$W_{18}O_{49}$ composite Electrodes

2.2.1 Synthesis of $W_{18}O_{49}$

No further purification was necessary for the chemicals because they were all high-grade. 2 g of tungsten hexachloride (WCl_6) dissolved in 50 ml of ethanol is enough to make one urchin-shaped sphere of $W_{18}O_{49}$ material; then, let the mixture stand at room temperature for 30 min while stirring. This procedure produces a solution that is both transparent and yellow. After that, the solution was moved to a 100 ml Teflon-lined stainless steel autoclave and subjected to a temperature of 160 ^oC for 24 h. A dark-blue solid was produced by centrifugation, followed by washing with ultra-pure water and ethanol. The next step was to dry the solid at 60^oC in a vacuum.

2.2.2 Synthesis of TiN

TiN nanobuds were produced by heating hydrothermally generated TiO_2 with ammonia for 3h. One mL of titanium butoxide (Ti $(C_4H_9O)_4$) was mixed with 30 mL of acetic acid. The solution was heated for 12 h at 140°C in a 50-mL Teflon stainless autoclave. The specimen was centrifuged numerous times in ethanol and DI water to remove contaminants. Drying at 60^oC for 24 h produced titanium dioxide (TiO_2). After that, TiO_2 was annealed at 800^oC for 3 h in 160 NH_3 scans.

2.2.3 Preparation of TiN-$W_{18}O_{49}$ Nanocomposite

The TiN-$W_{18}O_{49}$ heterostructured composite was prepared via a simple hydrothermal growth method and then heated. To make a stable suspension, 1 g of pre-synthesized TiN nanobuds was mixed with 50 ml of ethanol using ultra sonication for 30 minutes. To make the precursor solution for $W_{18}O_{49}$, 50 ml of ethanol were used to dissolve 2 g of WCl_6. After that, the $W_{18}O_{49}$ solution was slowly added to the TiN suspension, stirred constantly at room temperature for 30 minutes. This made a uniform mixture. After that, the mixture was heated for 24 h in a 100 mL stainless steel autoclave lined with Teflon at 160^oC. After cooling to room temperature, the dark-blue TiN-$W_{18}O_{49}$ nanocomposite was separated from the remaining material by centrifugation. It was cleaned several times with DI water and ethanol to remove any impurities, and then dried under vacuum at 60^oC. The heterostructure made by coupling TiN's excellent conductivity with $W_{18}O_{49}$'s pseudocapacitive activity increases the electrochemical performance of supercapacitors.

Table.1 Preparation conductions for TiN-$W_{18}O_{49}$ nanocomposite hetrostructure.

Materials	Precursors	Solvent	Synthesis Method	Time	Temperature

View Article Online
DOI: 10.1039/D6NA00134C

TiN-$W_{18}O_{49}$	TiN (1 g), WCl_2 (2g)	Ethanol (50 ml)	Hydrothermal	24 h	160°C

2.2.4 Electrode Preparation

The nickel foam was first washed using the following agents in the following order: acetone, 3 M HCl, 100% ethanol, and deionized water to ensure a clean surface before the electrode could be designed. The resulting slurry was coated onto a nickel foil substrate in spherical form using N-methyl-2-pyrrolidone as the solvent. The active material consisted of 80% synthesised material, 10% carbon black and 10% polyvinylidenedifluoride (PVDF). The electrode was subjected to 30 seconds of crushing at 30 MPa before being dried in a hot-air oven at 60 °C for 12 hours. The created electrode material had a mass of 2 mg.

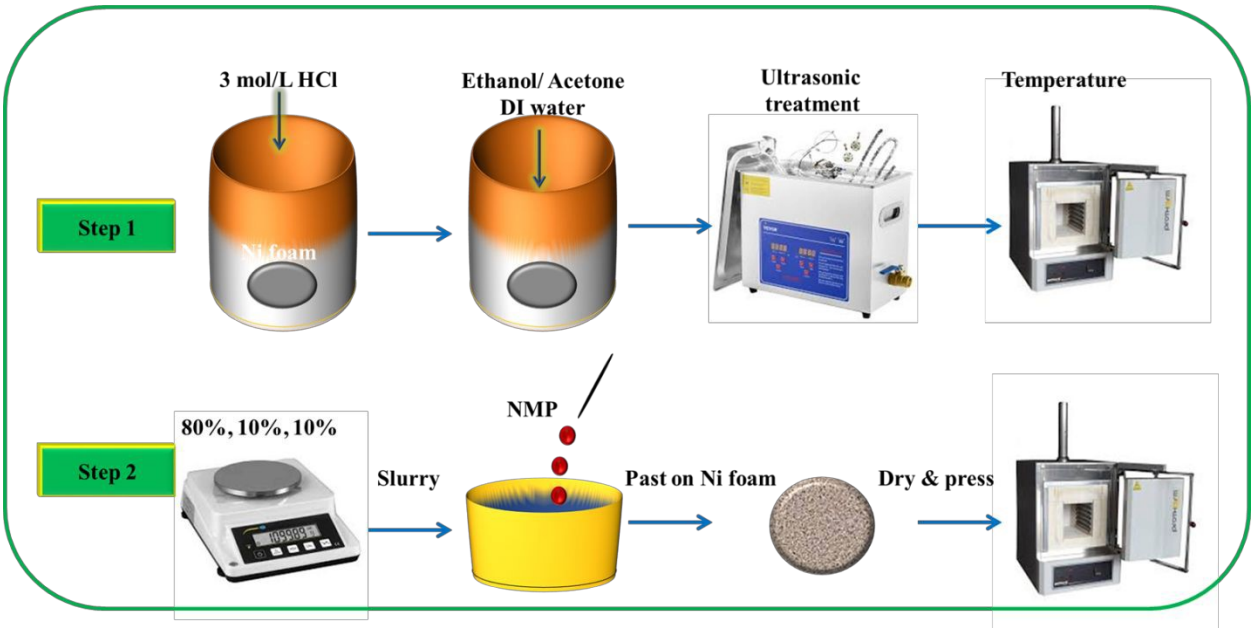

Scheme 1. Schematic diagram of preparation of Electrodes

2.3 Characterizations and Electrochemical Analysis

The crystalline characteristics of $W_{18}O_{49}$, TiN, and TiN-$W_{18}O_{49}$ nanocomposite were examined using CuKα radiation and a Rigaku D/max-A X-ray diffractometer (XRD) in an ambient environment within the 2θ range of 10° to 80°. We used a JEOL JSM-7800F FESEM (field-emission scanning electron microscopy) to examine the samples we made. Energy-dispersive X-

View Article Online
DOI: 10.1039/D6NA00134C

ray spectroscopy (EDS) was used to determine the elemental composition. A three-electrode system was employed on the DH7000C electrochemical workstation to evaluate the performance of electrode materials in an electrochemical environment. The reference electrode in the 3 E system was Ag/AgCl, and the counter electrode was platinum. All of this was in a 1 M KOH electrolyte solution. To make the working electrode, a homogenous slurry of the active material ($W_{18}O_{49}$, TiN, or TiN-$W_{18}O_{49}$ 80 wt %), carbon black (10 wt %), and polyvinylidene difluoride PVDF (10 wt %) was prepared in N-methyl-2-pyrrolidone (NMP) solvent. Then, a piece of Ni foam was used as the current collector, and the paste was baked in a vacuum oven at 60 ^{o}C for 24 h. We employed electrochemical impedance spectroscopy (EIS), galvanostatic charge-discharge (GCD), and cyclic voltammetry (CV) to examine the electrochemical properties of $W_{18}O_{49}$, TiN, and TiN-$W_{18}O_{49}$ nanocomposite over 0.1 Hz to 100 kHz. We employed galvanostatic charge-discharge (GCD) to measure the long-term cycling over 10,000 cycles at a current density of 10 $A{\cdot}g^{-1}$. We utilized the following equation to find the specific capacitances, energy densities, power densities, and Coulombic efficiencies of the active materials from their GCD analysis.

$$C_s = \frac{I \times \Delta t}{\Delta V} \quad (1)$$

$$E_d = \frac{C_s \times \Delta V^2}{7.2} \quad (2)$$

$$P_d = \frac{E_d \times 3600}{\Delta t} \quad (3)$$

$$\eta = \frac{T_d}{T_c} \times 100\% \quad (4)$$

In the above equations Cs is specific capacitance ($F{\cdot}g^{-1}$), I is current density ($A{\cdot}g^{-1}$), Δt is time (Sec), Ed is Energy density ($Wh{\cdot}Kg^{-1}$), ΔV is potential window (V), Pd is power density ($W{\cdot}Kg^{-1}$), and T_d and T_c is the time of discharge and charge respectively.

3. Results and Discussion

3.1 X rays Diffractions & BET analysis

The XRD pattern exhibits prominent peaks indicative of the monoclinic phase of $W_{18}O_{49}$. The (010), (002), (020), and (200) crystallographic planes of $W_{18}O_{49}$ correspond to the major diffraction peaks at 2θ values of approximately 23.2 ^{o}, 26.6 ^{o}, 34.1 ^{o}, and 48.1 ^{o}, respectively. These peaks have validated the $W_{18}O_{49}$ phase, consistent with JCPDS card No. 71-2450. The robust peaks in the diffraction pattern signify the structure of TiN. The (111), (200), (220), and (311) planes of TiN correspond to the peaks detected at 2θ values of approximately 36.6 ^{o}, 42.6 ^{o},

View Article Online
DOI: 10.1039/D6NA00134C

61.9 °, and 74.0 °, respectively. The peaks indicated by JCPDS No. 87-0632 confirm the crystallinity of TiN. The detection of peaks from both TiN and W18O49 in the XRD pattern confirms the successful formation of the TiN- $W_{18}O_{49}$ nanocomposite. Distinct peaks are observed at 36.6 ° and 42.6 °, corresponding to TiN, and at 23.2 ° and 26.6 °, corresponding to $W_{18}O_{49}$; no significant alterations or additional phases have been identified. This signifies that the TiN and $W_{18}O_{49}$ components amalgamated effectively without significant phase transformation and chemical contact, as their distinct crystal structures are maintained in the composite. Fig. 1b demonstrates that the BET analysis of the TiN-$W_{18}O_{49}$ nanocomposite reveals a substantial increase in surface area to 55.35 $m^2 \cdot g^{-1}$. The augmentation in surface area underscores the synergistic interaction between TiN and $W_{18}O_{49}$, leading to an enhanced availability of active sites for ion adsorption and optimized ion diffusion pathways. The increased surface area improves the electrochemical performance of the composite in supercapacitor applications.

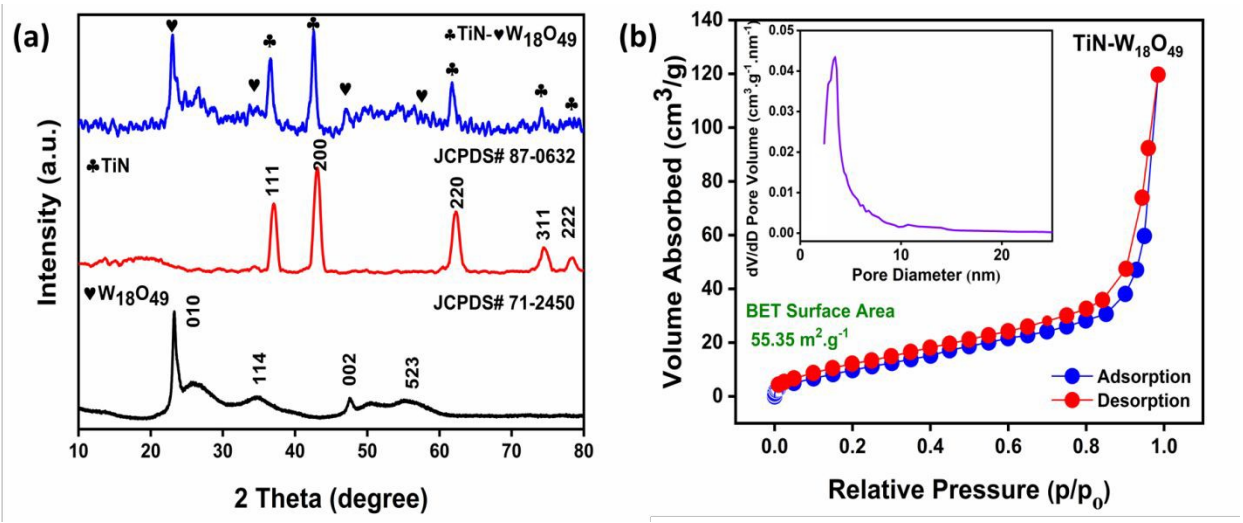

Fig.1 (a) X-rays diffraction of $W_{18}O_{49}$, TiN, and TiN-$W_{18}O_{49}$ nanocomposite, (b) BET analysis of TiN-$W_{18}O_{49}$ nano composite

3.2 Scanning Electron Microscopy and EDX with Mapping

The morphology of the TiN, $W_{18}O_{49}$, and TiN-$W_{18}O_{49}$ nanocomposite was examined via SEM, as illustrated in Fig 2. The SEM picture of TiN (Fig. 2a) displays a distinctive nano bud-like structure characterized by uniformly distributed spherical aggregates with little protrusions. These nanobuds establish a highly conductive network, which is optimal for improving charge

View Article Online
DOI: 10.1039/D6NA00134C

transfer in supercapacitor applications. A detailed examination (Fig. 2a$_1$) emphasizes the dense configuration of these buds, enhancing the material's mechanical stability and superior electrochemical characteristics. Conversely, $W_{18}O_{49}$ has a morphology resembling an urchin-like sphere (Fig. 2b), characterized by extending outward from a central core. This three-dimensional structure markedly augments the surface area, promoting improved ion adsorption and storage. At increased magnification (Fig. 2b$_1$), the distinct Urchin-like spheres prominently observable, highlighting the material's porosity characteristics, which are advantageous for ion transport and energy storage. The TiN-$W_{18}O_{49}$ nanocomposite (Fig. 2c) exhibits a cohesive hybrid architecture that integrates TiN nanobuds with $W_{18}O_{49}$ urchin-like spheres. This synergistic structure provides elevated conductivity and an extensive surface area, enhancing the material's electrochemical efficacy. The close-up image (Fig. 2c$_1$) illustrates the robust connection between the two phases, with the nano buds and urchin-like spheres creating a cohesive network, resulting in enhanced ion diffusion and charge storage capacities.

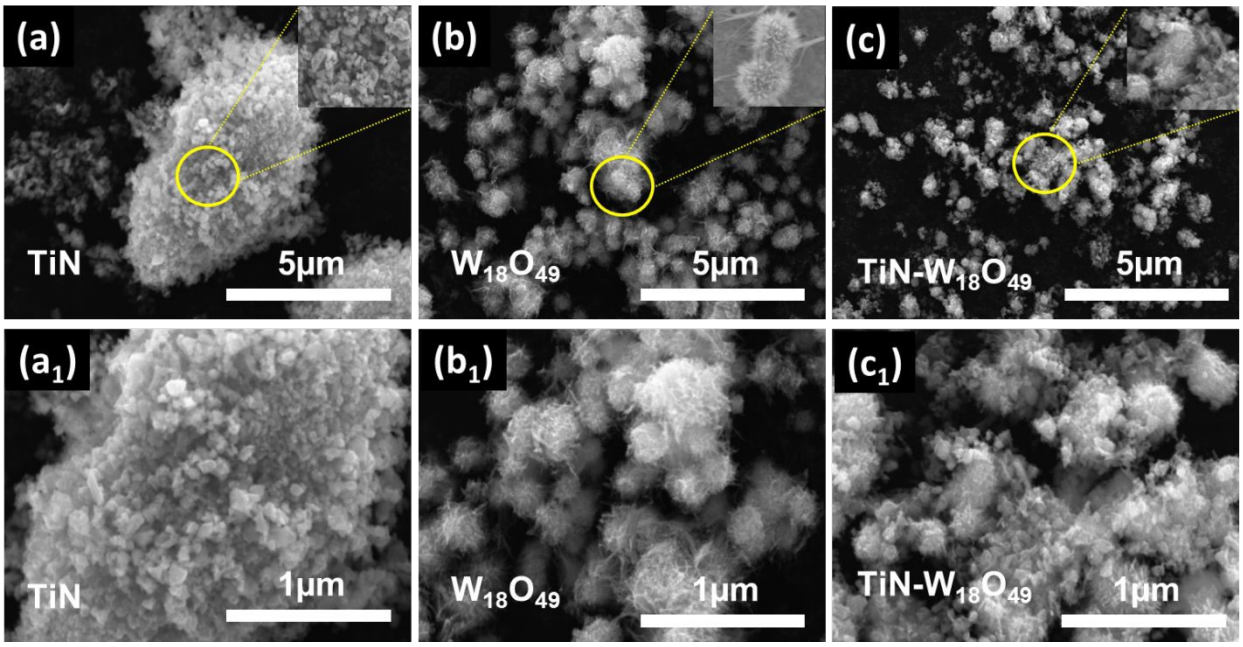

Fig.2 Scanning electron microscopy images of (a, a$_1$) TiN, (b, b$_1$) $W_{18}O_{49}$, and (c, c$_1$) TiN-$W_{18}O_{49}$ Nanocomposite

The EDX spectrum of the TiN-$W_{18}O_{49}$ nanocomposite (Fig. 3a) exhibits peaks for Ti, N, W, and O, thereby validating the effective amalgamation of the two constituents. The presence of these components in appropriate ratios signifies composite creation and the lack of contaminants, indicating a well-integrated hybrid structure. The EDS mapping of the TiN-$W_{18}O_{49}$

View Article Online
DOI: 10.1039/D6NA00134C

nanocomposite (Fig. 3b) demonstrates the homogeneous distribution of Ti, N, W, and O inside the material. This uniform distribution of components indicates a robust interaction between the TiN and $W_{18}O_{49}$ phases, facilitating effective charge transfer and ion storage inside the composite. The uniform distribution of TiN and $W_{18}O_{49}$ enhances the material's electrochemical performance by reducing conductive routes and offering several active sites for ion adsorption.

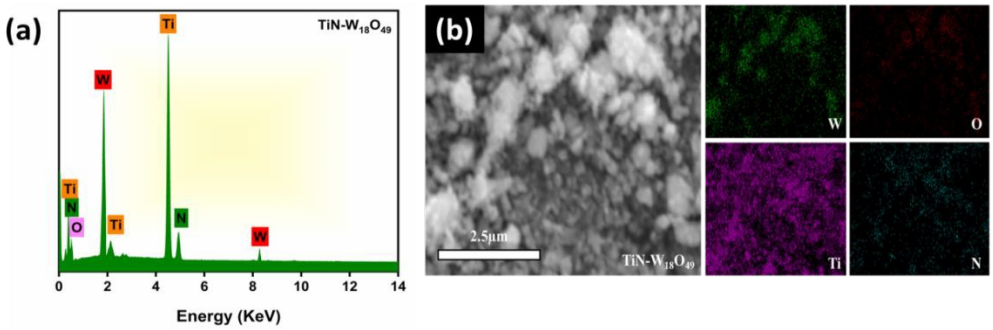

Fig.3 (a) EDX analysis of TiN-$W_{18}O_{49}$ nanocomposite, and (b) EDS mapping

4. Electrochemical performance of prepared electrodes in three-electrode system

4.1 Cyclic Voltammetry (CV) Analysis

Figure. 4(a-c) shows the CV curves for the $W_{18}O_{49}$, TiN, and TiN-$W_{18}O_{49}$ nanocomposite electrodes. The scan speeds ranged from 10-50 $mV{\cdot}s^{-1}$, and the potential window ranged from 0-0.5 V (Ag/AgCl as the reference electrode). The mixed charge-storage mechanism in the $W_{18}O_{49}$ electrode is mainly made up of surface pseudocapacitance from reversible W^{6+}/W^{5+} redox processes and partial electric double-layer capacitance (EDLC). The CV profiles of this electrode are almost rectangular, with weak redox humps (Fig. 4a). The current response, which increases with the scan rate, shows that ions can easily go back and forth, indicating good electrochemical reversibility. Fig. 4b shows that the TiN electrode exhibits a low current density and a steady CV shape, as it is a metal conductor with an enormous EDLC contribution and a negligible Faradaic contribution. TiN does not play a significant role as a redox-active component; rather, it primarily serves as an efficient electron transport channel. The TiN and $W_{18}O_{49}$ nanocomposite, on the other hand, has better pseudocapacitive behavior, with a broader contained CV zone and more obvious redox features (Fig. 4c). The quick electron transport of TiN and the many redox-active sites of $W_{18}O_{49}$ work together to make this improvement happen. The composite structure enables fast ion diffusion and improved charge-transfer kinetics. Fig. 4d shows the CV curves of $W_{18}O_{49}$, TiN, and TiN- $W_{18}O_{49}$ nanocomposite at a constant scan rate of 20 $mV{\cdot}s^{-1}$.

View Article Online
DOI: 10.1039/D6NA00134C

The composite electrode has a much higher current density than its individual parts, which shows that the better electrochemical performance is attributable to electronic interaction and interfacial coupling between TiN and $W_{18}O_{49}$ and not just an extra effect. This link stabilizes redox processes and makes electrical conductivity better throughout cycling. So the charge-storage kinetics by observing at the slope (b-value) in Fig. 4e, which shows how log (i) and log (v) are related. The TiN-$W_{18}O_{49}$ nanocomposite electrode is closer to 1 than either $W_{18}O_{49}$ (0.632) or TiN (0.698) since its b-value is 0.789. Thus, a surface-controlled pseudocapacitive mechanism, rather than a diffusion-limited faradaic reaction, regulates the composite electrode. A higher b-value indicates a faster rate and a faster charge response. Fig. 4f shows that both diffusion and surface processes happen at the same time in the composite electrode. It also shows that the anodic and cathodic peak currents are directly related to the square root of the scan rate ($V^{1/2}$). During cycling, both the anodic and cathodic peak currents grow symmetrically. This shows that redox processes are highly reversible and that stable ions are added or removed. The surface redox reactions involved during the charge storage mechanism are:

$$TiN + OH^- \leftrightarrow TiNOH + e^- \quad (5)$$

At the high potential, the oxidation occurred like

$$TiN + 2OH^- \leftrightarrow TiO + NH^- + H_2O + e^- \quad (6)$$

While the storage behavior of W18O49 involved following reactions

$$W_{18}O_{49} + xOH^- + xe^- \leftrightarrow W_{18}O_{49-x}(OH)_x \quad (7)$$

$$W^{6+} + e^- \leftrightarrow W^{5+} \quad (8)$$

$$TiN + W_{18}O_{49} + xOH^- \leftrightarrow TiN^* + W_{18}O_{49-x}(OH)_x + xe^- \quad (9)$$

The charge is kept in the TiN-$W_{18}O_{49}$ composite by a combination of surface pseudocapacitance and fast electron movement between the interfaces. TiN has highly conductive routes and can participate in reversible surface redox processes with OH ions. $W_{18}O_{49}$, on the other hand, largely contributes through W^{6+}/W^{5+} redox reactions that happen with OH^- adsorption /intercalation. The close TiN-$W_{18}O_{49}$ nanocomposite hetero-interface improves capacitance, rate capability, and cycling stability by facilitating rapid electron transport, lowering charge-transfer resistance, and enabling better use of electro active sites.

View Article Online
DOI: 10.1039/D6NA00134C

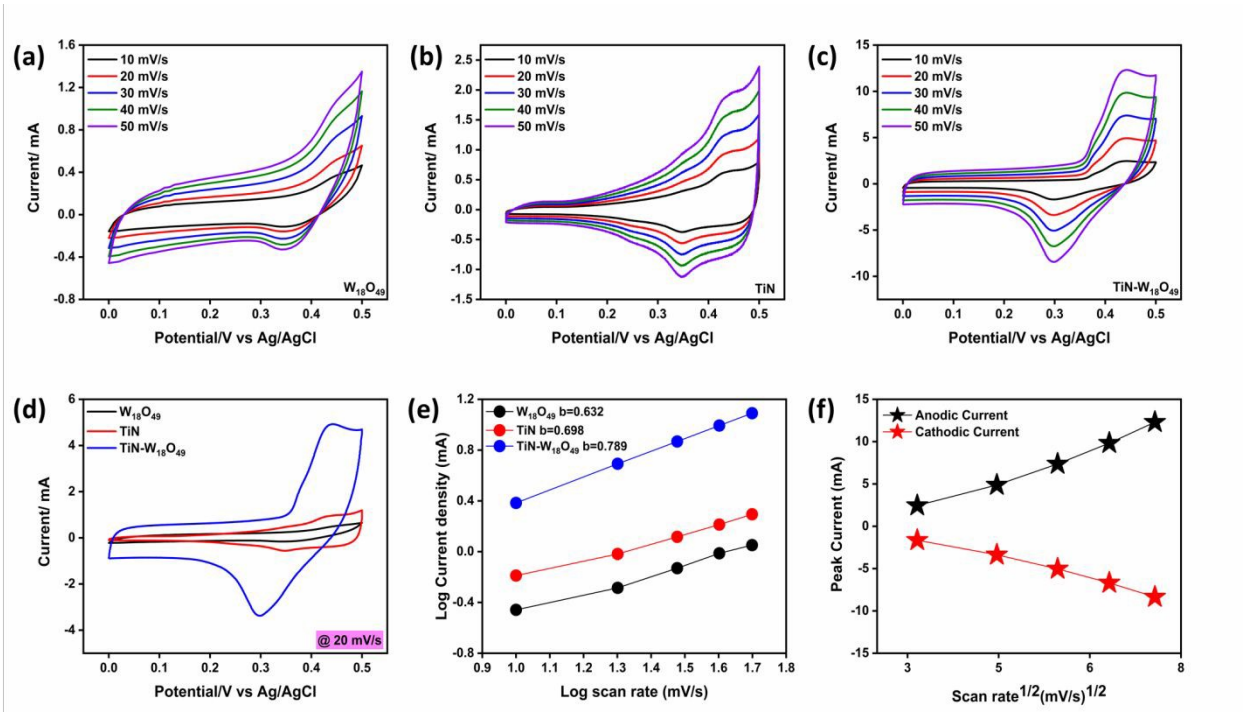

Fig.4 Cyclic voltammetry analysis of, (a) $W_{18}O_{49}$, (b) TiN, (c) TiN-$W_{18}O_{49}$ nanocomposite at scan rate of 10-50 mV·s^{-1}, (d) Comparative analysis of all electrodes at 20 mV·s^{-1}, (e) b value, and (f) Peak current plot

4.2 Electrochemical Surface Area (*ECSA*) and Interfacial Charge Storage Mechanism

Figure 5(a-d) compares the electrochemical surface area (*ECSA*) of $W_{18}O_{49}$, TiN, and the TiN-$W_{18}O_{49}$ nanocomposite electrodes using cyclic voltammetry experiments. The *ECSA* values indicate the number of charge-storage active sites that are electrochemically accessible. They are based on the capacitive current response at scan rates between 10- 50 mV·s^{-1}. Fig. 5a shows that the *ECSA* ($\approx$0.22 mF cm^{-2} at 50 mV·s^{-1}) of the TiN-$W_{18}O_{49}$ nanocomposite is substantially greater than that of TiN and $W_{18}O_{49}$ purely. The composite architecture allows the electrolyte to reach more electrochemically active sites due to this significant gain. The synergistic interfacial contact between TiN and $W_{18}O_{49}$ prevents particle aggregation, creates a large number of hetero surfaces, and makes the electrolyte more wet able. All of these things boost *ECSA*. Fig. 5(b-d) demonstrate how the *ECSA* changes with the scan rate for the $W_{18}O_{49}$, TiN, and TiN-$W_{18}O_{49}$ nanocomposite electrodes. When scan rates increases, *ECSA* increases steadily across all electrodes. These results show that surface sites are being activated more slowly and that ions are more readily accessible. The oxygen-deficient $W_{18}O_{49}$ shows surface-controlled redox activity, as seen in Fig. 5b. Most of the time, reversible W^{6+}/W^{5+} redox events occur near the surface. Still,

View Article Online
DOI: 10.1039/D6NA00134C

the relatively low absolute *ECSA* indicates limited electrical conductivity and that the active sites are only used part of the time. In Fig. 5c TiN shows a slight increase in *ECSA* with scan rate, which is expect from a material with metallic conductivity and charge storage primarily due to electric double-layer capacitance (EDLC). Even though it has excellent electron transport, its overall *ECSA* is limited because there aren't any strong Faradaic reactions. The TiN-$W_{18}O_{49}$ nanocomposite has the highest absolute *ECSA* and the steepest increase of all the scan rates (Fig. 5d). This behavior shows that TiN serves as a scaffold that carries electrons, accelerating the movement of charges to the active sites in TiN-$W_{18}O_{49}$, on the other hand, has a lot of redox-active centers. The surfaces being so close together lets electrons and ions move quickly between them, making the most of the active sites already there. The chemical reason the TiN-$W_{18}O_{49}$ nanocomposite has a higher *ECSA* is that it contains oxygen vacancies, which increase the electronic density and accelerate surface redox processes. The interface between TiN and $W_{18}O_{49}$ exhibits strong electronic coupling, lowering the charge-transfer barrier and facilitating electron mobility. Because the electrochemically active interface is larger, electrolyte ions can reach deeper surface areas without diffusing. These behaviors work together to create a pseudocapacitive process that occurs primarily at the surface. In this process, charge storage is regulated by reversible redox reactions rather than slow bulk diffusion. The TiN-$W_{18}O_{49}$ electrode has a much greater *ECSA*, which gives it its high specific capacitance and rate capabilities. Increasing the size of the *ECSA* improves both energy storage efficiency and cycling stability. This is because it promises more active sites for charge accumulation and faster kinetics.

View Article Online
DOI: 10.1039/D6NA00134C

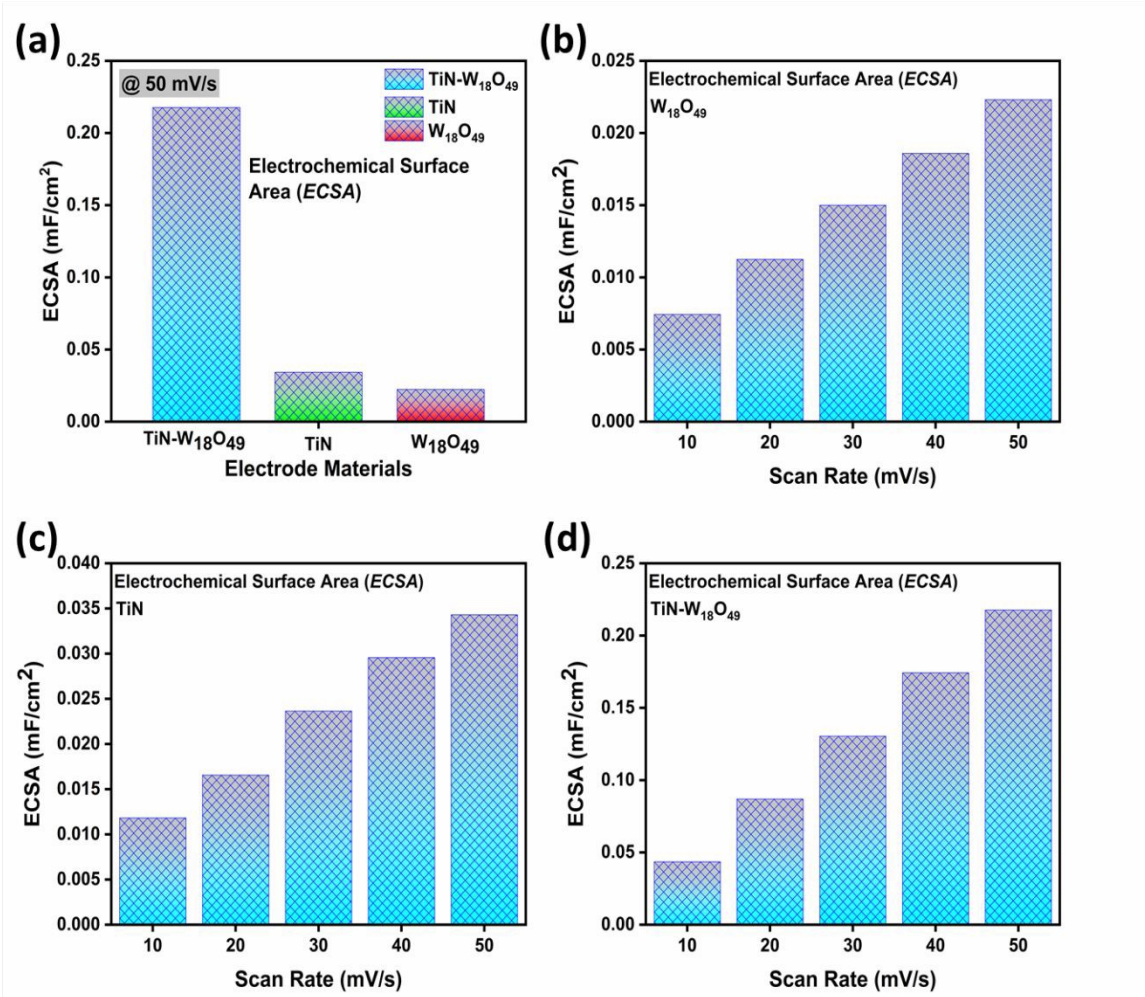

Fig.5 (a) Electrochemical surface area of all electrodes at 50 $mV \cdot s^{-1}$, (b) $W_{18}O_{49}$, (c) TiN, and (d) TiN-$W_{18}O_{49}$ nanocomposite at 10-50 $mV \cdot s^{-1}$

Table.2 Electrochemical active surface area of $W_{18}O_{49}$, TiN, and TiN-$W_{18}O_{49}$ nanocomposite at 1-5 $A \cdot g^{-1}$

Scan Rate ($mV \cdot s^{-1}$)	Electrochemical Active Surface Area ($mF \cdot cm^{-2}$)		
	$W_{18}O_{49}$	TiN	TiN-$W_{18}O_{49}$
10	0.00744	0.01182	0.04353
20	0.01125	0.01656	0.08696
30	0.01500	0.02366	0.13045
40	0.01859	0.02957	0.17425
50	0.02231	0.03431	0.21769

4.3 Capacitive Diffusion Contribution

View Article Online
DOI: 10.1039/D6NA00134C

To quantitatively clarify the charge-storage kinetics of $W_{18}O_{49}$, TiN, and TiN- $W_{18}O_{49}$ nanocomposite electrodes, the capacitive and diffusion-controlled contributions were examined by a power-law connection between current (i) and scan rate (v):

$$i(V) = av^b \qquad (10)$$

Where *a,* and *b* are constants that can be changed. The value of *b* shows what the main way to store charge is: To further differentiate the current response at a specific potential, the total current was delineated using the equation:

$$i(V) = k_1 v + k_2 v^{1/2} \qquad (11)$$

Where: $k_1 v$ represents the surface capacitive contribution (including EDLC and fast surface redox), $k_2 v^{1/2}$ corresponds to diffusion-controlled faradaic processes.

By fitting CV curves at different scan rates $W_{18}O_{49}$ shows that the diffusion contribution decreases from 91 % to 73 %, while the capacitive contribution starts at 09 % at 10 $mV{\cdot}s^{-1}$ and increases to 27 % at 50 $mV{\cdot}s^{-1}$. The redox transitions of W^{6+}/W^{5+} are linked to the bulk intercalation and deintercalation of electrolyte ions into the $W_{18}O_{49}$ lattice, which is where this phenomenon starts. At higher scan speeds, the storage process changes slightly to surface-controlled reactions, since there isn't enough time for deep ion diffusion. Fig. 6b shows that as the scan rate increases from 10 to 50 $mV{\cdot}s^{-1}$, TiN's capacitive contribution increases from 13 % to 33 %. This is more than $W_{18}O_{49}$'s contribution. The diffusion factor also drops from 87 % to 67 %. This improvement is due to TiN's metallic conductivity and surface-dominant charge storage, which primarily lead to charge accumulation via shallow redox reactions and rapid surface adsorption. But the presence of a diffusion contribution means that some of the electrolyte ions that come close to the surface participate.

The capacitive contribution of the TiN-$W_{18}O_{49}$ composite (Fig. 6c) rises from 27 % at 10-50 $mV{\cdot}s^{-1}$, while the diffusion contribution drops from 73 % to 49 %. This activity confirms a charge-storage mechanism in which TiN provides a highly conductive network for rapid electron transport, while $W_{18}O_{49}$ offers redox-active sites and the capacity to intercalate ions. The hetero-interface shortens ion-diffusion pathways and speeds up surface redox kinetics. Scanning at

View Article Online
DOI: 10.1039/D6NA00134C

higher rates shows better rate capability because capacitive processes are more critical than diffusion-limited processes. In Fig. 6d, the shaded area shows the capacitive current and the total CV response at 50 $mV{\cdot}s^{-2}$ for the TiN-$W_{18}O_{49}$ nanocomposite electrode. The broad overlap between total and capacitive currents supports the idea that surface-controlled processes store more than 50 % of the charge at high scan speeds, which is consistent with the 51 % capacitive contribution.

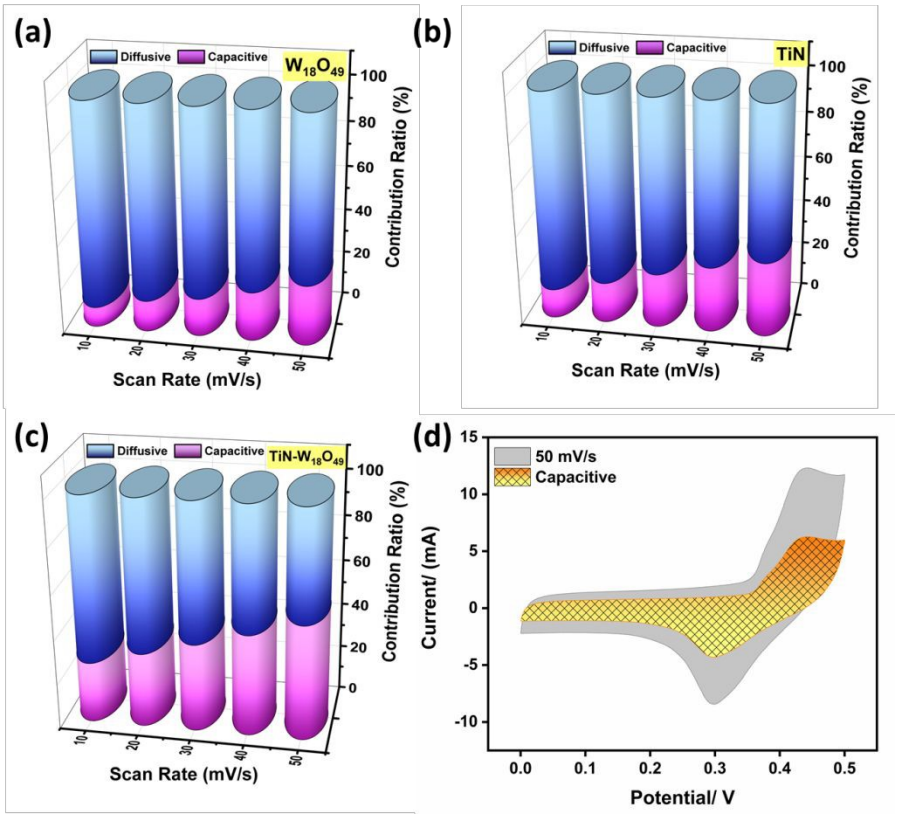

Fig.6 (a-c) Capacitive-Diffusion analysis of $W_{18}O_{49}$, TiN, and TiN-$W_{18}O_{49}$ nanocomposite at 10-50 $mV{\cdot}s^{-1}$, (d) Capacitive behavior of TiN-$W_{18}O_{49}$ nanocomposite at 50 $mV{\cdot}s^{-1}$

Table.3 Capacitive diffusive contribution of $W_{18}O_{49}$, TiN, and TiN-$W_{18}O_{49}$ nanocomposite at 10-50 $mV{\cdot}s^{-1}$

Scan Rates ($mV{\cdot}s^{-1}$)	$W_{18}O_{49}$		TiN		TiN-$W_{18}O_{49}$	
	Cap (%)	Diff (%)	Cap (%)	Diff (%)	Cap (%)	Diff (%)
10	09	91	13	87	27	73
20	14	86	18	82	33	67
30	17	83	24	76	39	61
40	22	78	29	71	45	55

View Article Online
DOI: 10.1039/D6NA00134C

50	27	73	33	67	51	49

4.4 Electrochemical Impedance Spectroscopy (EIS)

Figure.7(a-b) shows the Nyquist plots of the $W_{18}O_{49}$, TiN, and TiN-$W_{18}O_{49}$ nanocomposite electrodes. These graphs show the interfacial charge-transfer behavior and ion transport kinetics. All electrodes exhibit a small semicircle in the high-frequency region and an inclined line in the low-frequency region. This suggests that charge-transfer resistance and ion diffusion processes work together. The high-frequency intercept on the real axis shows that the solution resistance (R_s) is 0.45 Ω for $W_{18}O_{49}$, 0.50 Ω for TiN, and 0.54 Ω for TiN-$W_{18}O_{49}$ nanocomposite. This means the electrodes have about the same resistance to contact and to the electrolyte. The TiN-$W_{18}O_{49}$ heterostructure has a semicircle diameter of just 1.38 Ω, which is much lower than the diameters of TiN (2.50 Ω) and $W_{18}O_{49}$ (3.89 Ω). The composite electrode exhibits much faster interfacial electron-transport kinetics. When oxygen-vacancy-rich $W_{18}O_{49}$ and highly conductive TiN come into contact with each other, they create efficient electron transport channels and lower interfacial polarization, which lowers R_{ct}. The steeper low-frequency region for TiN-$W_{18}O_{49}$ also indicates better capacitive performance and shorter ion diffusion paths, as the electrolyte is easier to reach. In short, the TiN-$W_{18}O_{49}$ heterostructures better rate capability and electrochemical performance are due to its better electrochemical kinetics, which are shown by its lower charge-transfer resistance, similar solution resistance, and better ion transport.

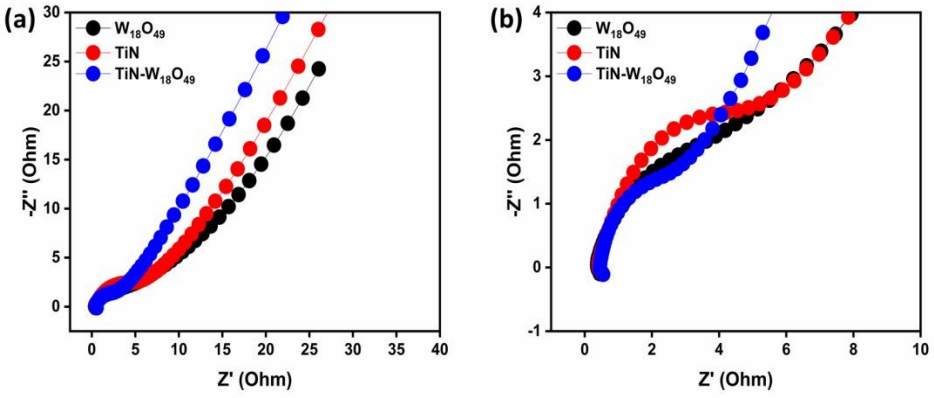

Fig.7 (a) EIS plot of $W_{18}O_{49}$, TiN, and TiN-$W_{18}O_{49}$ nanocomposite, (b) Zoom view

Table.4 R_s and R_{ct} calculation from EIS data

Electrodes	**$W_{18}O_{49}$**	**TiN**	**TiN-$W_{18}O_{49}$**

View Article Online
DOI: 10.1039/D6NA00134C

$\mathbf{R_s}$	0.45	0.50	0.54
$\mathbf{R_{ct}}$	3.89	2.50	1.38

4.5 Galvanostatic Charge discharge (GCD)

Figure. 8(a-d) shows the GCD curves for the $W_{18}O_{49}$, TiN, and TiN-$W_{18}O_{49}$ nanocomposite electrodes. The curves were recorded at 1-5 $A{\cdot}g^{-1}$ within a potential range of 0-0.5 V (versus Ag/AgCl). Using the GCD profiles can help to better understand the reversibility, charge-storage kinetics, and internal electrochemical mechanisms. The TiN-$W_{18}O_{49}$ electrode exhibits a longer discharge time at 3 $A{\cdot}g^{-1}$ than the other two electrodes, indicating a higher specific capacitance (Fig. 8a). The $W_{18}O_{49}$ electrode exhibits a shorter discharge time and a nonlinear voltage profile, typical of pseudocapacitive behaviour driven by reversible W^{6+}/W^{5+} redox processes. The electric double-layer capacitance (EDLC)-dominated behaviour of TiN is substantiated by its relatively symmetric and linear GCD curves, arising from its metallic conductivity and limited redox activity, which distinguish it from other materials. Fig. 8(b-d) show the GCD curves for $W_{18}O_{49}$, TiN, and TiN-$W_{18}O_{49}$ at current densities of 1 to 5 $A{\cdot}g^{-1}$.

As the current density increases, the charge-discharge time decreases for all electrodes. This is because ions don't diffuse as well at greater rates. Interestingly, the TiN-$W_{18}O_{49}$ nanocomposite (Fig. 8d) keeps quasi-symmetrical GCD patterns even at high current densities. This suggests that the charge moves quickly and that the material can be reversibly electrochemically modified. The low internal resistance is due to the rapid ion exchange at the $W_{18}O_{49}$ surface and the efficient electron transport through the TiN network, as shown by the maintained discharge shape and the lower IR drop. Fig. 8e shows how specific capacitance and current density are related. The TiN-$W_{18}O_{49}$ nanocomposite electrode exhibits the highest particular capacitance across all current densities and maintains most of its initial capacitance even at 5 $A{\cdot}g^{-1}$. The improved rate performance is due to the higher electrical conductivity of TiN, the many redox-active sites of $W_{18}O_{49}$, and the shorter ion transport pathways that come from strong interfacial contact. $W_{18}O_{49}$ has a lower rate capability because its conductivity limits its rate, while TiN has a moderate capacitance because it doesn't undergo significant Faradaic reactions. Fig. 8f shows the coulombic efficiency of each electrode at different current densities. The TiN-$W_{18}O_{49}$ nanocomposite has very few parasitic reactions and charge-discharge cycles that are very easy to reverse. Its coulombic efficiency is always close to one. This stability is due to the strong hetero

View Article Online
DOI: 10.1039/D6NA00134C

interface, which prevents structural damage and irreversible redox reactions during cycling. Table 5 shows the results of the rate capability test on the electrodes, which were measured at current densities ranging from 1 to 5 $A{\cdot}g^{-1}$. The $W_{18}O_{49}$ electrode has a specific capacitance of 238 $F{\cdot}g^{-1}$ at 1 $A{\cdot}g^{-1}$, but this value slowly reduces to 110 $F{\cdot}g^{-1}$ at 5 $A{\cdot}g^{-1}$. This shows that the electrode has low electrical conductivity and only partially uses redox-active sites at higher rates. The TiN electrode, on the other hand, exhibits higher capacitance, with 742 $F{\cdot}g^{-1}$ at 1 $A{\cdot}g^{-1}$ and 506 $F{\cdot}g^{-1}$ at 5 $A{\cdot}g^{-1}$. This is because it has good metallic conductivity and efficient charge transport. The TiN-$W_{18}O_{49}$ nanocomposite exhibits the highest specific capacitance of all the current densities tested. It reaches 1482 $F{\cdot}g^{-1}$ at 1 $A{\cdot}g^{-1}$ and stays at 860 $F{\cdot}g^{-1}$ even at 5 $A{\cdot}g^{-1}$. The composite electrode's better rate performance shows how TiN and $W_{18}O_{49}$ work together. TiN allows electrons to move quickly, and $W_{18}O_{49}$ has many redox-active sites, which improve charge storage and rate stability.

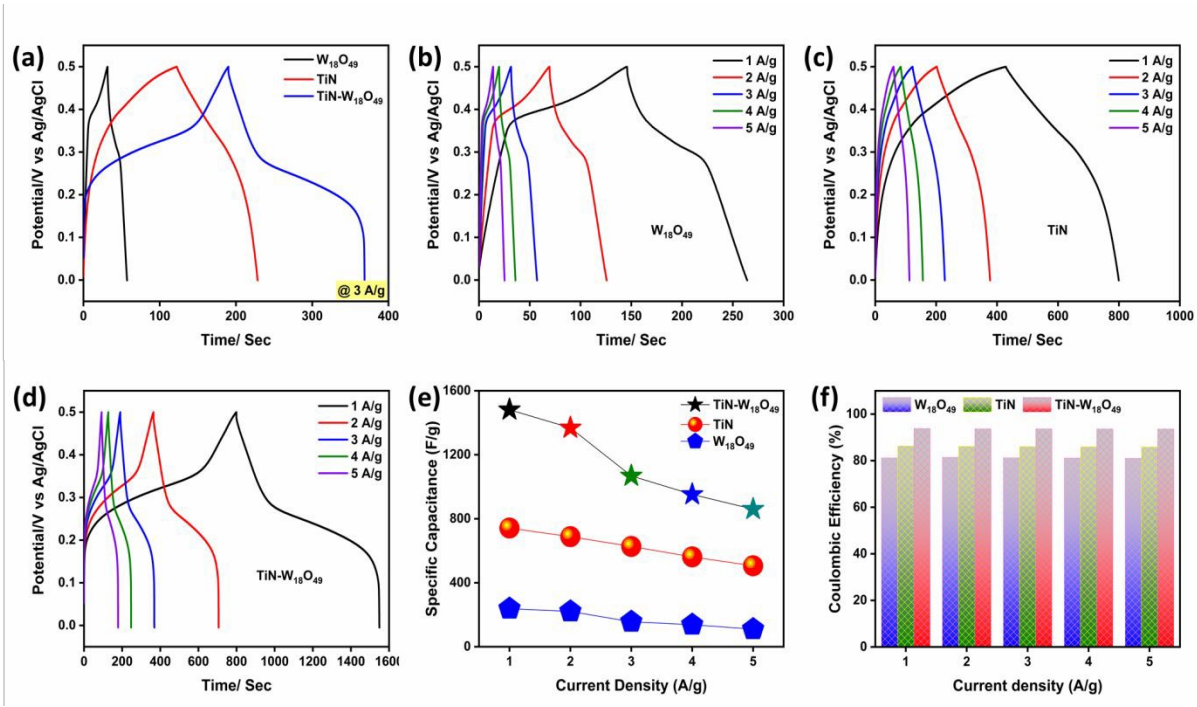

Fig.8 Galvanostatic Charge-Discharge comparison of $W_{18}O_{49}$, TiN, TiN-$W_{18}O_{49}$ at 3 $A{\cdot}g^{-1}$, (b) $W_{18}O_{49}$, (c) TiN, (d) TiN-$W_{18}O_{49}$ nanocomposite at 1-5 $A{\cdot}g^{-1}$, (e) Specific capacitance, (f) Coulombic Efficiency at 1-5 $A{\cdot}g^{-1}$

Table.5 Specific capacitance calculations from GCD graphs of $W_{18}O_{49}$, TiN, and TiN-$W_{18}O_{49}$ nanocomposite at 1 to 5 $A{\cdot}g^{-1}$

View Article Online
DOI: 10.1039/D6NA00134C

Current density ($A \cdot g^{-1}$)	Specific capacitance		
	$W_{18}O_{49}$ ($F \cdot g^{-1}$)	TiN ($F \cdot g^{-1}$)	TiN-$W_{18}O_{49}$ ($F \cdot g^{-1}$)
1	238	742	1482
2	221	688	1368
3	156	627	1068
4	138	562	952
5	110	506	860

Table.6 The coulombic efficiency of $W_{18}O_{49}$, TiN, and TiN-$W_{18}O_{49}$ nanocomposite from 1 to 5 $A \cdot g^{-1}$

Current density ($A \cdot g^{-1}$)	Coulombic Efficiency (%)		
	$W_{18}O_{49}$	TiN	TiN-$W_{18}O_{49}$
1	81.26	86.36	93.84
2	81.50	86.19	93.70
3	81.29	86.12	93.70
4	81.18	86.02	93.67
5	81.06	85.92	93.65

5. Asymmetric Device (TiN-$W_{18}O_{49}$//AC)

The asymmetric supercapacitor device depicted schematically in Fig. 9a, functions within a broader voltage range of 1.3 V and comprises a positive electrode made of TiN-$W_{18}O_{49}$ nanocomposite and a negative electrode consisting of activated carbon (AC). There are holes in the $W_{18}O_{49}$ lattice that are involved in surface redox reactions, and the very conductive TiN moves the electrons to the outside circuit. When ions flow toward both electrodes simultaneously, the electric double-layer capacitance (EDLC) at the AC electrode and pseudocapacitive faradaic processes at the TiN-$W_{18}O_{49}$ nanocomposite electrode work together to store charge. This charge input significantly improves the process of building the total charge. Fig. 9b illustrates the cyclic voltammetry (CV) curves for the TiN-$W_{18}O_{49}$//AC asymmetric device at 10 $mV \cdot s^{-1}$. The device shows a steady, asymmetric CV over a wide voltage range of 1.3 V, indicating that the asymmetric supercapacitor assembly functioned. The TiN-$W_{18}O_{49}$ nanocomposite electrode's dominant pseudocapacitive activity makes it seem very different from an ideal rectangular form. This is because of reversible redox reactions between W^{+6}/W^{+5} couples and surface-confined reactions that are helped by oxygen vacancies. The AC electrode primarily enables rapid charge adjustment by functioning as an EDLC. The CV curves in Fig. 9c were made by scanning at

View Article Online
DOI: 10.1039/D6NA00134C

speeds of 10-100 $mV \cdot s^{-1}$. Keeping the curve's shape at high scan rates means that ions move quickly, and the rate capacity is high. The enhanced current response with increasing scan rate indicates that electrons can move rapidly through the TiN conductive framework and that electrolyte ions can quickly reach the active $W_{18}O_{49}$ sites. In pseudocapacitive systems, a small amount of polarization is expected at higher scan speeds due to diffusion-limited kinetics. Fig. 9d shows galvanostatic charge-discharge (GCD) curves for different current densities (1-7 $A \cdot g^{-1}$). The quasi-triangular profiles with modest voltage plateaus provide more evidence for the existence of EDLC and faradaic charge storage mechanisms. The more active sites are used up when discharge times are longer, and current densities are lower. The discharge time decreases as the current density increases because deep redox-active areas are harder to reach and ion diffusion is limited. Fig. 9e shows (Table 7), the device has a high specific capacitance of 251.5 $F \cdot g^{-1}$ at 1 $A \cdot g^{-1}$; however, this drops to 83.3 $F \cdot g^{-1}$ at 7 $A \cdot g^{-1}$. Because only sites accessible from the surface can contribute to charge storage at higher current densities, kinetic limitations account for a significant part of the capacitance decay. Fig. 9f shows the results of electrochemical impedance spectroscopy (EIS). The narrow intercept on the real axis indicates that TiN has good electrical contact and high intrinsic conductivity. This also reveals that the internal resistance (R_s) is low. The nearly vertical line in the low-frequency zone indicates that ions can move easily and that capacitive behaviour is optimal. The rapid faradaic kinetics at the TiN-$W_{18}O_{49}$ nanocomposite interface is corroborated by the absence of a discernible semicircle, signifying that the charge-transfer barrier is insignificant.

View Article Online
DOI: 10.1039/D6NA00134C

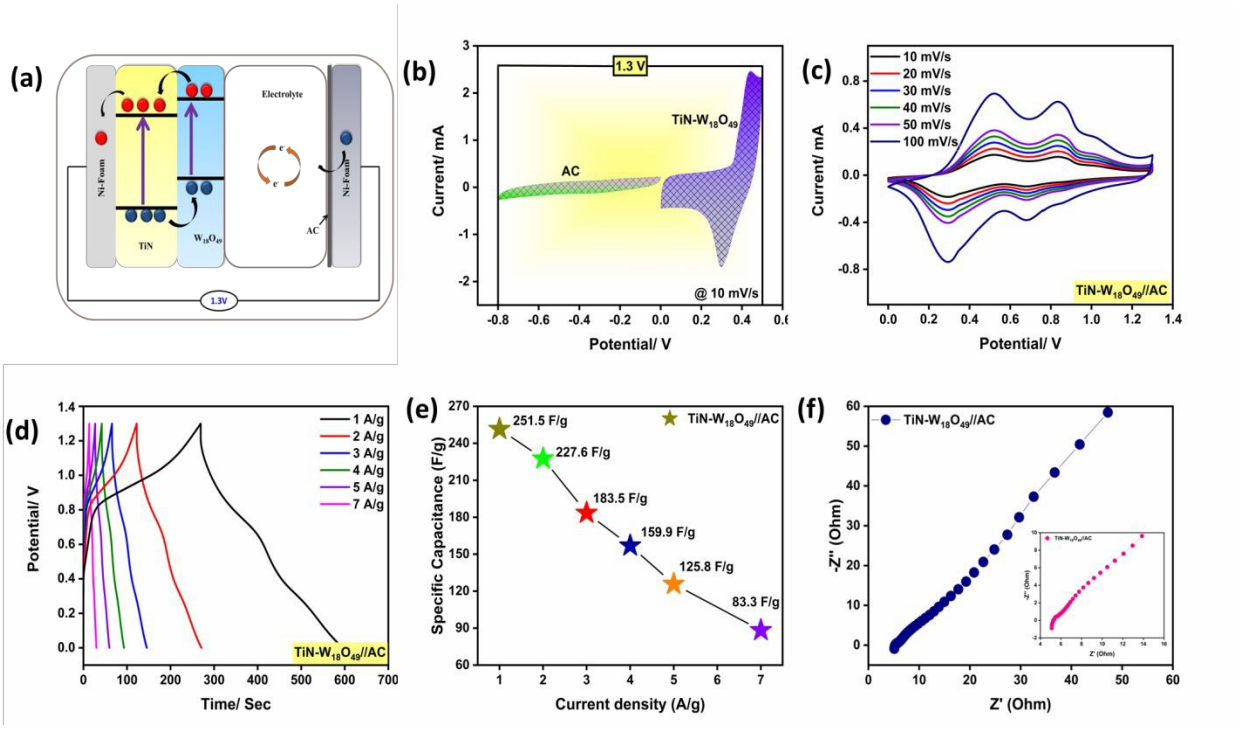

Fig.9 (a) Asymmetric supercapacitor TiN-$W_{18}O_{49}$//AC device, (b) CV window of TiN-$W_{18}O_{49}$ and AC, (c) CV analysis at 10-100 $mV{\cdot}s^{-1}$, (d) GCD results of TiN-$W_{18}O_{49}$//AC at 1-7 $A{\cdot}g^{-1}$, (e) Specific capacitance *vs* current density, and (f) EIS plot

Table.7 Specific capacitance, Energy density, and Power density calculated from TiN-$W_{18}O_{49}$//AC asymmetric device

Current density ($A{\cdot}g^{-1}$)	Specific Capacitance ($F{\cdot}g^{-1}$)	Energy density ($Wh{\cdot}kg^{-1}$)	Power density ($W{\cdot}kg^{-1}$)
1	251.5	58.91	648.5
2	227.6	53.42	1290.6
3	183.5	43.06	1962.2
4	159.9	36.80	2597.6
5	125.8	29.52	3187.6
7	83.3	20.72	4564.9

Figure. 10a shows the Ragone plot of the TiN-$W_{18}O_{49}$//AC asymmetric supercapacitor for different current densities. It highlights the trade-off between power density and energy density. The device can offer a high energy density of 58.91 $Wh{\cdot}kg^{-1}$ at a power density of 648.5 $Wh{\cdot}kg^{-1}$, even at a low current density of 1 $A{\cdot}g^{-1}$. This is because it uses the active material efficiently and gives the electrolyte ions enough time to reach redox-active sites. As the current density

View Article Online
DOI: 10.1039/D6NA00134C

increases from 2 to 7 $A{\cdot}g^{-1}$, the energy density decreases from 53.42 to 20.72 $Wh{\cdot}kg^{-1}$. On the other hand, the power density goes up from 1290.6 to 4564.9 $W{\cdot}kg^{-1}$. Due to kinetic limitations, the inverse correlation between the two variables intensifies at elevated current densities: diffusion-controlled faradaic processes are inhibited, and surface-dominated charge storage is preferred. The device has an excellent rate capability, even at a high power density of 3187.6 $W{\cdot}kg^{-1}$ (5 $A{\cdot}g^{-1}$), and it keeps a good energy density of 29.52 $Wh{\cdot}kg^{-1}$. The material's excellent performance is due to the combined effects of TiN's highly conductive electron transport network and $W_{19}O_{49}$'s redox-active sites and pseudocapacitance generated by oxygen vacancies. An AC negative electrode in an asymmetrical design immediately increases energy density by widening the working voltage window, as demonstrated by:

$$E = \frac{1}{2}CV^2 \qquad (12)$$

In above equation E is energy density, C is the device capacitance, and V is the operating voltage. Fig. 10b shows how stable the TiN-$W_{18}O_49$//AC asymmetric device is over time when a high current density of 10 $A{\cdot}g^{-1}$ is used. The device's ability to retain 91.1 % of its original capacitance after 10,000 charge-discharge cycles demonstrates strong electrochemical endurance. After a slight decline at the beginning of each cycle, capacitance stabilizes. This is generally explained by electrode activation and electrolyte wetting. This means that the process of storing charge is very reversible. The TiN-$W_{18}O_{49}$ nanocomposite is strong enough to prevent excessive volume changes during ion insertion and removal. Efficient charge equilibrium between the electric double-layer AC negative electrode and the pseudocapacitive positive electrode, alongside robust interfacial coupling between TiN and $W_{18}O_{49}$, ensures stable electron pathways and inhibits material degradation.

View Article Online
DOI: 10.1039/D6NA00134C

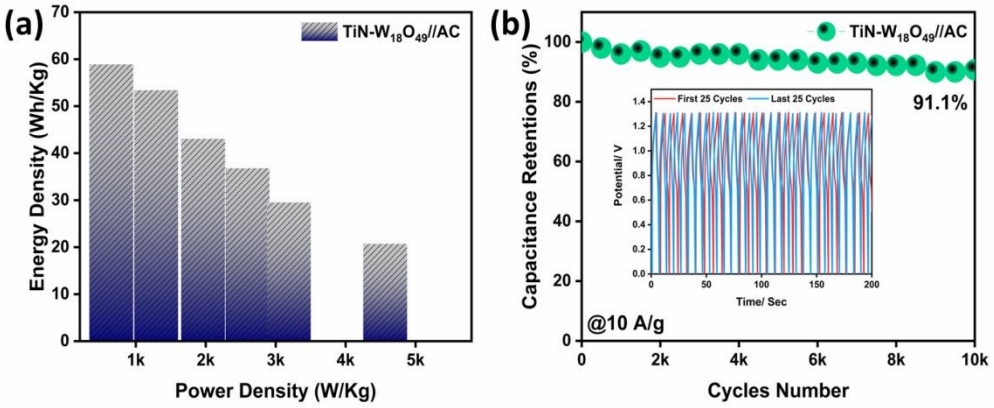

Fig.10 (a) Energy density *vs* Power density, (b) Capacitance retention of TiN-$W_{18}O_{49}$//AC at 10 $A{\cdot}g^{-1}$

Table.8 Comparative electrochemical performance of electrodes material based on tungsten composite materials

Materials	Specific Capacitance ($F{\cdot}g^{-1}$)	Current density (A/g)/ Scan Rate	Potential Window (V)	Retention (%) @ No of Cycles	Ref.
$CoWO_4$	378	2 mV/s	-0.3 to 0.4	95@4000	[29]
Urchin like $W_{18}O_{49}$	315	1	-0.5 to 0.4	110@7000	[30]
$W_{18}O_{49}$@C	588.3	1	-0.4 to 0.4	88@ 5000	[31]
WO_3 microspher	797.05	0.5	-0.35 to 0.2	100.47@2000	[32]
WO_3/PANI	168	1.28 mA/cm^2	0.5 to 0.7	60@1000	[33]
Ti/IrO_2/WO_3	46	20 mV/s	0.2 to 1.2	50@100	[34]
OMC/WO_{3-x}	175	2 mV/s	-0.2 to 0.7	N/A	[35]
$Sm_2(WO_4)_3$	326	2 mV/s	-0.4 to 0.4	90@4000	[36]
$W_{18}O_{49}$ nanowires/ PANI	440	2	-0.6 to 0.2	N/A	[37]
Graphene nanosheets-WO_3	143.6	0.1	0.0 to 1	N/A	[38]
ZnS-$W_{18}O_{49}$	517	1	-0.1 to 0.0	98.1@10,000	[39]
TiN-$W_{18}O_{49}$	1482	1	0.0 to 0.5	91.1@10,000	**This Work**

6. Conclusion

A TiN-$W_{18}O_{49}$ nanocomposite heterostructured electrode was successfully produced and extensively studied for high-performance supercapacitor applications. Structural and morphological analyses validated the creation of the heterostructure, integrating the superior electrical conductivity of TiN with the pseudocapacitive properties of $W_{18}O_{49}$. Electrochemical investigations revealed that the TiN-$W_{18}O_{49}$ nanocomposite markedly surpasses its constituent elements, displaying minimal solution resistance (R_s = 0.54 Ω) and diminished charge transfer

View Article Online
DOI: 10.1039/D6NA00134C

resistance (R_{ct} = 1.38 Ω), signifying effective electron transport and improved interfacial kinetics. The prepared electrodes exhibited distinct redox peaks in cyclic voltammetry (0.0-0.5 V, 10-50 $mV{\cdot}s^{-1}$) and attained a substantial specific capacitance of 1482 $F{\cdot}g^{-1}$ at 1 $A{\cdot}g^{-1}$ in three electrode system. The asymmetric supercapacitor TiN-$W_{18}O_{49}$//AC device maintained 91.1 % of retention after 10,000 cycles, achieving a maximum energy density of 58.91 $Wh{\cdot}Kg^{-1}$ and a power density of 4564.9 $W{\cdot}Kg^{-1}$. The results underscore the synergistic interaction between TiN and $W_{18}O_{49}$, positioning the heterostructure as a suitable electrode material for advanced high-performance supercapacitors.

Author statement: This is author original work and is not being submitted or considered anywhere else for possible publication.

Compliance with ethical standards

The authors declare that they have no conflict of interest.

Declaration of interests

The authors declare that they have no known competing financial interests or personal relationships that could have appeared to influence the work reported in this paper.

Author contributions statement:

Junaid Riaz: Wrote the original manuscript draft, Data curation, Characterization. Muhammad Arif: writing-review & editing, Methodology. Amina Bibi: Formal analysis, Software. Salah Knani: Conceptualization, Supervision.

Acknowledgement

The authors extend their appreciation to the Deanship of Scientific Research at Northern Border University, Arar, KSA for funding this research work through the project number "NBU-FFR-2026-2483-01"

View Article Online
DOI: 10.1039/D6NA00134C

References:

[1] Riaz, Junaid, Yongguo Zhang, Jianchun Cao, Amina Bibi, Zhengyun Zhang, and Xiaolong Zhou. "High-performance electrode material synthesis via wet-chemical method: a study on NbN–Fe2O3 composite." *Journal of Materials Science: Materials in Electronics* 35, no. 17 (2024): 1176.

[2] Anshu, Satvik, Shyamal Shegokar, R. Rahul, Lalit Bharti, and Amreesh Chandra. "Reinforced carbon nanofiber porous network for large-area aqueous supercapacitors achieving 2.3 V without using water-in-salt type electrolyte." Chemical Engineering Journal (2025): 171505.

[3] Riaz, Junaid, Jianchun Cao, Yongguo Zhang, Amina Bibi, and Xiaolong Zhou. "Facile synthesis and electrochemical analysis of TiN-based ZnO nanoparticles as promising cathode materials for asymmetric supercapacitors." Nanoscale Advances 6, no. 20 (2024): 5145-5157.

[4] Xiong, Chuanyin, and Yadong Su. "Recent Progress of Transition Metal-Based Oxide Composite Electrode Materials in Supercapacitor." Advanced Sustainable Systems 9, no. 1 (2025): 2400578.

[5] Xu, Guangxu, Hang Yin, Jianmin Zhang, Fengyun Wang, Naoki Fukata, and Jie Tang. "Designing of metal Ru doped amorphous RuO2/Graphene for high performance supercapacitor." Journal of Alloys and Compounds (2025): 182082.

[6] Kumar, Subramanian Ashok, Thiruppathi Govindhan, Karuppaiah Selvakumar, Kareem Yusuf, Shanmugam Mahalingam, Tae Hwan Oh, Subramaniyan Ramasundaram, and Junghwan Kim. "Fabrication of N-doped ZnO for evaluation of photocatalytic degradation of methylene blue, methyl orange and improved supercapacitor efficiency under redox-active electrolyte." Materials Science in Semiconductor Processing 186 (2025): 109052.

[7] Arif, Muhammad, Junaid Riaz, Hongran Yang, Zhaoming Fu, Amina Bibi, and Ting Zhu. "Synthesis of high-performance CdS/MnO composite electrode to achieve high energy and power densities for asymmetrical supercapacitors." Materials & Design 251 (2025): 113704..

[8] Boutaleb, Nadia, Ghadah M. Al-Senani, Salhah D. Al-Qahtani, Abdelghani Benyoucef, and B. Dhygham Alkoudsi. "Investigation and properties of PAni-coated CuO–ZnO–MnO quaternary hybrid as electrode material for supercapacitor application." Colloids and Surfaces A: Physicochemical and Engineering Aspects 718 (2025): 136867.

[9] Wang, Meilong, Linsong Li, Zhentao Liu, Fuzhong Wu, Huixin Jin, Yi Wang, and Siyu Cai. "Multicomponent Co2O3@ CoMo2S4 Core–Shell Structures as a Binder-Free Electrode for Cycling Stability Supercapacitors." ACS omega 10, no. 9 (2025): 8901-8910..

[10] Mohan, Visakh V., P. M. Anjana, and R. B. Rakhi. "One pot synthesis of tungsten oxide nanomaterial and application in the field of flexible symmetric supercapacitor energy storage device." Materials Today: Proceedings 62 (2022): 848-851.

View Article Online
DOI: 10.1039/D6NA00134C

[11] Li, Muyun, Haoyang Yan, Honglong Ning, Xinglin Li, Jinyao Zhong, Xiao Fu, Tian Qiu, Dongxiang Luo, Rihui Yao, and Junbiao Peng. "Application of tungsten-oxide-based electrochromic devices for supercapacitors." Applied System Innovation 5, no. 4 (2022): 60.

[12] Li, Ruidong, Baoquan Liang, Hong Gao, Jie Li, Qianwen Liu, Lihua Chen, Shuxin Song, Bingyue Zheng, Tingxi Li, and Yong Ma. "Fabrication of binder-free MXene/reduced graphene oxide/W18O49 film electrode for flexible supercapacitors." Journal of Energy Storage 106 (2025): 114741.

[13] Pan, Zhihu, Chenghao Yang, Zhiwu Chen, and Xiaohong Ji. "Construction of Ti3C2T x/WO x heterostructures on carbon cloth for ultrahigh-mass loading flexible supercapacitor." Nano Research 15, no. 10 (2022): 8991-8999.

[14] Patil, Amar M., Jiajia Wang, Shasha Li, Xiaoqiong Hao, Xiao Du, Zhongde Wang, Xiaogang Hao, Abuliti Abudula, and Guoqing Guan. "Bilateral growth of monoclinic WO3 and 2D Ti3C2Tx on 3D free-standing hollow graphene foam for all-solid-state supercapacitor." Chemical Engineering Journal 421 (2021): 127883.

[15] Thalji, Mohammad R., Gomaa AM Ali, Porun Liu, Yu Lin Zhong, and Kwok Feng Chong. "W18O49 nanowires-graphene nanocomposite for asymmetric supercapacitors employing AlCl3 aqueous electrolyte." Chemical Engineering Journal 409 (2021): 128216..

[16] Li, Yanmei, Jin Hu, Zhongshan Deng, Huachao Huang, Zheng Liu, Jiaxin Fu, Kaijun Wang, Kaizhao Wang, Yongjin Feng, and Weijun Zhang. "Sn-doped three-dimensional sea urchin-like morphology of W18O49 marterials for supercapacitor." Journal of Materials Science: Materials in Electronics 36, no. 4 (2025): 1-13.

[17] Riaz, Junaid, Fawad Aslam, Muhammad Arif, Tabasum Huma, and Amina Bibi. "First investigation of high-performance FeS-based W 18 O 49 asymmetric supercapacitors operating at 1.6 V." Nanoscale Advances 7, no. 1 (2025): 231-241.

[18] Tong, Haiyun, Zhaoxiaorong Nan, Hanlu Zhang, Bingbing Yang, Yingjie Liu, Peiqi Guo, Yiyong Wei, Zhenfa Zi, and Xuebin Zhu. "Synthesis and performance of TiN film electrode for supercapacitor by a facile chemical solution deposition method." Journal of Materials Science: Materials in Electronics 35, no. 2 (2024): 182.

[19] Sharma, Siddharth, Ravikant Adalati, Nitesh Choudhary, B. S. Unnikrishnan, Meenakshi Sharma, P. Gopinath, and Ramesh Chandra. "Physiological fluid based flexible NbN|| TiN supercapacitor for biocompatible energy storage applications." Journal of Alloys and Compounds 960 (2023): 170749.

[20] Lu, Xihong, Gongming Wang, Teng Zhai, Minghao Yu, Shilei Xie, Yichuan Ling, Chaolun Liang, Yexiang Tong, and Yat Li. "Stabilized TiN nanowire arrays for high-performance and flexible supercapacitors." Nano letters 12, no. 10 (2012): 5376-5381.

View Article Online
DOI: 10.1039/D6NA00134C

[21] Sial, Qadeer Akbar, Ranveer Singh, Shahid Iqbal, Rubaya Yeasmin, Young-Jae Lee, Shankara S. Kalanur, and Hyngtak Seo. "A multifunctional TiN/Ni electrode for wearable supercapacitor and sensor with an insight into charge storage mechanism." Applied Surface Science 555 (2021): 149718.

[22] Qi, Hualei, Samuel Yick, Oskar Francis, Adrian Murdock, Timothy van der Laan, Kostya Ken Ostrikov, Zheng Bo, Zhaojun Han, and Avi Bendavid. "Nanohybrid TiN/Vertical graphene for high-performance supercapacitor applications." Energy Storage Materials 26 (2020): 138-146.

[23] Arif, Muhammad, Junaid Riaz, Amina Bibi, Hongran Yang, and Ting Zhu. "Enhancing supercapacitor energy density by TiN–ZnS composites unveiled as a promising electrode." APL Materials 12, no. 7 (2024).

[24] Riaz, Junaid, Jianchun Cao, Yongguo Zhang, Amina Bibi, Muhammad Arif, Zhengyun Zhang, Dost Muhammad, and Xiaolong Zhou. "Improved performance of TiN nano buds decorated MoS2 sheets in asymmetric supercapacitors." Journal of Materials Science: Materials in Electronics 35, no. 17 (2024): 1142.

[25] Riaz, Junaid, Yongguo Zhang, Jianchun Cao, Amina Bibi, Muhammad Arif, Zhengyun Zhang, Dost Muhammad, and Xiaolong Zhou. "Facile synthesis of TiN nano sheets decorated Fe2O3 nanoparticles as novel cathode material for Asymmetric Supercapacitor." Surfaces and Interfaces 46 (2024): 104080.

[26] Riaz, Junaid, Wang Yongyuan, Jianchun Cao, Amina Bibi, Dost Muhammad, Hassna Eman, and Xiaolong Zhou. "Wet-chemical synthesized TiN-CuO nanocomposite: Advancing supercapacitor technology with high energy and power density." *Physica E: Low-dimensional Systems and Nanostructures* 165 (2025): 116105.

[27] Riaz, Junaid, Jianchun Cao, Nadimullah Hakimi, Anila Sikandar, Fawad Aslam, Tabasum Huma, and Amina Bibi. "Synthesis of high-performance supercapacitor electrode materials by wet-chemical route based on TiN–Al 2 O 3 composite." *Journal of Materials Science: Materials in Electronics* 36, no. 35 (2025): 2257.

[28] Ren, Peng, Chao Chen, and Xiuchun Yang. "Nanostrucutured MnO2-TiN nanotube arrays for advanced supercapacitor electrode material." Scientific Reports 12, no. 1 (2022): 2088.

[29] Adib, Kourosh, Mehdi Rahimi-Nasrabadi, Zolfaghar Rezvani, Seied Mahdi Pourmortazavi, Farhad Ahmadi, Hamid Reza Naderi, and Mohammad Reza Ganjali. "Facile chemical synthesis of cobalt tungstates nanoparticles as high performance supercapacitor." *Journal of Materials Science: Materials in Electronics* 27, no. 5 (2016): 4541-4550.

[30] Park, Sangbaek, Hyun-Woo Shim, Chan Woo Lee, Hee Jo Song, Jae-Chan Kim, and Dong-Wan Kim. "High-power and long-life supercapacitive performance of hierarchical, 3-D urchin-like W18O49 nanostructure electrodes." *Nano Research* 9, no. 3 (2016): 633-643.

View Article Online
DOI: 10.1039/D6NA00134C

[31] Jung, Jinjoo, and Do Hyung Kim. "W18O49 nanowires assembled on carbon felt for application to supercapacitors." *Applied Surface Science* 433 (2018): 750-755.

[32] Xu, Juan, Taotao Ding, Jin Wang, Jun Zhang, Shuai Wang, Changqing Chen, Yanyan Fang, Zhihao Wu, Kaifu Huo, and Jiangnan Dai. "Tungsten oxide nanofibers self-assembled mesoscopic microspheres as high-performance electrodes for supercapacitor." *Electrochimica Acta* 174 (2015): 728-734.

[33] Zou, Ben-Xue, Ying Liang, Xiao-Xia Liu, Dermot Diamond, and King-Tong Lau. "Electrodeposition and pseudocapacitive properties of tungsten oxide/polyaniline composite." *Journal of Power Sources* 196, no. 10 (2011): 4842-4848.

[34] Ren, Xiu-Bin, Hai-Yan Lu, Hai-Bo Lin, Ya-Nan Liu, and Yan Xing. "Preparation and characterization of the Ti/IrO2/WO3 as supercapacitor electrode materials." *Russian Journal of Electrochemistry* 46, no. 1 (2010): 77-80.

[35] Zhou, Yuanyuan, Seunghyun Ko, Chul Wee Lee, Sung Gyu Pyo, Soo-Kil Kim, and Songhun Yoon. "Enhanced charge storage by optimization of pore structure in nanocomposite between ordered mesoporous carbon and nanosized WO3− x." *Journal of Power Sources* 244 (2013): 777-782.

[36] Sobhani-Nasab, Ali, Hamid Naderi, Mehdi Rahimi-Nasrabadi, and Mohammad Reza Ganjali. "Evaluation of supercapacitive behavior of samarium tungstate nanoparticles synthesized via sonochemical method." *Journal of Materials Science: Materials in Electronics* 28, no. 12 (2017): 8588-8595.

[37] Tian, Yuyu, Shan Cong, Wenming Su, Hongyuan Chen, Qingwen Li, Fengxia Geng, and Zhigang Zhao. "Synergy of W18O49 and polyaniline for smart supercapacitor electrode integrated with energy level indicating functionality." *Nano letters* 14, no. 4 (2014): 2150-2156.

[38] Cai, Yun, Yan Wang, Shaojuan Deng, Gang Chen, Qing Li, Bingqian Han, Rong Han, and Yude Wang. "Graphene nanosheets-tungsten oxides composite for supercapacitor electrode." *Ceramics International* 40, no. 3 (2014): 4109-4116.

[39] Riaz, Junaid, Jianchun Cao, Amina Bibi, Muhammad Arif, and Dost Muhammad. "Hydrothermal synthesis of ball-like ZnS nanospheres decorated urchin-like W18O49 nanospheres as electrode for high power and stable hybrid supercapacitor." *Materials Letters* 370 (2024): 136853.

View Article Online
DOI: 10.1039/D6NA00134C

Data availability

"The data supporting this article have been included as part of the Supplementary Information".